

Object Wake-up: 3D Object Reconstruction and Animation from a Single Image

Xinxin Zuo^{*,†} Ji Yang^{*} Sen Wang^{*,†} Priyal Belgamwar[§] Zhenbo Yu[‡]
 Xingyu Li^{*} Bingbing Ni^{‡,‡} Minglun Gong[†] Li Cheng^{*}
^{*}University of Alberta [‡]Shanghai Jiao Tong University [‡]Huawei Hisilicon
[†]University of Guelph [§]Pune Institute of Computer Technology
 xzuo, jyang7, sen9, xingyu, lcheng5@ualberta.ca

Abstract

Given a single chair image, could we extract its 3D shape and animate its plausible articulations and motions? This is an interesting new question that may have numerous downstream augmented reality and virtual reality applications. In this paper, we propose an automated approach to tackle the entire process of reconstruct such 3-D generic objects from single images, rigging and animation. Comparing with previous efforts on object manipulation, our work goes beyond 2D manipulation. Moreover, we endow plausible human-like or animal-like deformations to the otherwise rigid-body objects such as chairs; this leads to greater flexibility in terms of feasible object motions. Empirically our approach is demonstrated with satisfactory performance on public datasets as well as our in-house dataset; when compared on the related tasks of 3D reconstruction and skeleton prediction, our results surpass those of the State-of-the-arts by a noticeable margin. Our implementation and dataset are to be made publicly available upon paper acceptance.

1. Introduction

Presented with a single image of a generic object, say an airplane or a chair, our goal is to reconstruct its 3D shape, rig, and animate its plausible and possibly fun motions, such as an airplane flapping its wings or a chair walking as a quadruped, as illustrated in Fig. 1. This new question considered in this paper essentially entails the extraction and manipulation of objects from images, which could have many downstream applications in virtual reality or augmented reality scenarios. It is worth noting that there has been research efforts [14] performing 3D manipulations from a single input image, where the main focus is on rigid transformations. To create non-rigid deformations, professional software has been relied on with intensive user interactions. Instead, we aim to automate the entire pipeline of object reconstruction, rigging, and animation. The ob-

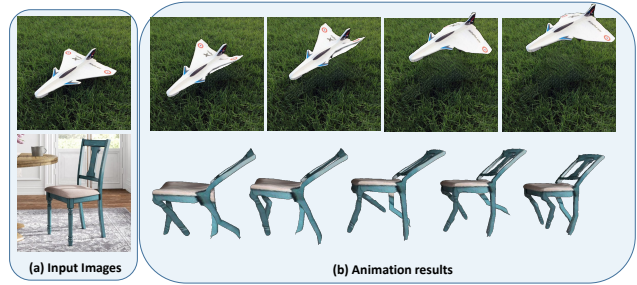


Figure 1. Two exemplar results. Given an input image of airplane or chair, our approach is capable of *reconstructing* its 3D shape, *rigging* and *animating* its plausible bird-like or quadruped-like motions.

jects, as we considered here, are articulated – objects that are capable of being controlled by a set of joints. In a sense, our problem could be considered as a generalization of image-based 3D reconstruction and animation of humans to generic objects encountered in our daily life, as long as they could be endowed with a skeleton.

Compared with the more established topic of human body animation [39], there are nevertheless new challenges to tackle with. To name one, there is no pre-existing parametric shape model for general objects. Besides, the human template naturally comes with its skeletal configuration for 3D motion control, and the precise skinning weights designed by professionals. However, such skeletal joints are yet to be specified not to mention the skinning weights in the case of generic objects, which usually have complex and diverse structures.

These observations have motivated us to propose an automated pipeline consisting of three steps. Step one involves 3D shape reconstruction from a single image. It includes a transformer-based [33] encoder as the feature extractor, followed by an occupancy prediction module and an auxiliary voxel prediction module with improved loss function [20]. Step two focuses on predicting both the skeletal joints and bones as estimating the multi-head probability field, inspired by the deep implicit functions of [20]. Specif-

ically, compared with previous rigging methods with voxel-based [43] or mesh-based representations [42], we are able to predict the existence probability of joints and bones in a continuous 3D space. To further improve the performance, a joint-aware instance segmentation is proposed and incorporated as an auxiliary task that considers the regional features of neighboring points. Finally, step three is to animate the rigged 3D shape following source motions from e.g. humans and animals. Our focus in this paper is mainly on the first two steps.

Our contributions are listed as follows: 1) a new object wake-up problem is considered. For which an automated pipeline is proposed to reconstruct, rig, and animate the 3D objects of interest from single images. To our knowledge, it is the first attempt to deform and articulate generic objects from images; 2) As essential components in our 3-step pipeline, a transformer-based occupancy network is developed to reconstruct 3D shapes from images. In particular, a novel and effective skeleton prediction approach with a multi-head structure is developed by utilizing the deep implicit functions. Moreover, in-house datasets (SSkel & ShapeRR) of general 3D objects are constructed, containing annotated 3D skeletal joints and photo-realistic re-rendered images, respectively. Empirically our entire pipeline is shown to achieve satisfactory results. Further evaluations on the public benchmarks and on our in-house datasets demonstrate the superior performance of our approach on the related tasks of image-based shape reconstruction and skeletal joint prediction.

2. Related Work

Image-based Object Reconstruction. There exist numerous studies on image-based 3D object reconstruction with various 3D shape representations, including voxel, octree [28, 32, 37], deep implicit function, mesh and point cloud [8, 17, 21, 27]. Methods based on different representations have their own benefits and shortcomings. For example, as a natural extension of 2D pixels, voxel representation [9, 35] has been widely used in early efforts due to its simplicity of implementation and compatibility with the convolutional neural network. However, these approaches often yield relatively coarse results, at the price of significant memory demand and high computational cost. Mesh-based representations [12, 15, 19, 36], on the other hand, become more desirable in real applications, as they are able to model fine shape details, and are compatible with various geometry regularizers. It is however still challenging to work with topology changes [24, 36]. Deep implicit 3D representations [5, 18, 25, 34] have recently attracted wide attention as a powerful technique in modeling complex shape topologies at arbitrary resolutions.

Skeleton Prediction and Rigging. The task of skeleton prediction has been investigated in various fields and

utilized in a variety of applications for shape modeling and analysis. The best-known example is the medial axis [1, 2], which is an effective means for shape abstraction and manipulation. Curve skeleton or meso-skeleton [11, 44] have been popular in computer graphics, mostly due to their compactness and ease of manipulation. It is worth noting the related research around detecting 3D keypoints from input point clouds, such as skeleton merger [30].

Pinocchio [3] is perhaps the earliest work on automatic rigging, which fits a pre-defined skeletal template to a 3D shape, with skinning obtained through heat diffusion. These fittings, unfortunately, tend to fail as the input shapes become less compatible with the skeletal template. On the other hand, hand-crafting templates for every possible structural variation of an input character is cumbersome. More recently, Xu et al. [43] propose to learn a volumetric network for inferring skeletons from input 3D characters, which however often suffers from the limited voxel resolution. Exploiting the mesh representation, RigNet [42] utilizes a graph neural network to produce the displacement map for joint estimation, which is followed by the additional graph neural networks to predict joint connectivity and skinning weights. Its drawback is they assume strong requirements for the input mesh such as a watertight surface with evenly distributed vertices can be satisfied. Besides, they predict the joints and kinematic chains successively causing error propagation from stages.. In contrast, a deep implicit function representation [20] which is capable of predicting the joints and bones over a continuous 3D space is considered in this paper for inferring skeleton.

Image based Object Animation. An established related topic is photo editing, which has already been popular with professional tools such as PhotoShop. Existing tools are however often confined to 2D object manipulations in performing basic functions such as cut-and-paste and hole-filling. A least-square method is considered in [29] to affine transform objects in 2D. The work of [10] goes beyond linear transformation, by presenting an as-rigid-as-possible 2D animation of a human character from an image, it is however manual intensive. In [41], 2D instances of the same visual objects are ordered and grouped to form an instance-based animation of non-rigid motions. Relatively few research activities concern 3D animations, where the focus is mostly on animals, humans, and human-like objects. For example, photo wake-up [39] considers reconstruction, rig, and animate 3D human-like shapes from input images. This line of research benefits significantly from the prior work establishing the pre-defined skeletal templates and parametric 3D shape models for humans and animals. On the other hand, few efforts including [14] consider 3D manipulations of generic objects from images, meanwhile, they mainly focus on rigid transformations. Our work could be regarded as an extension of automated image-based human shape recon-

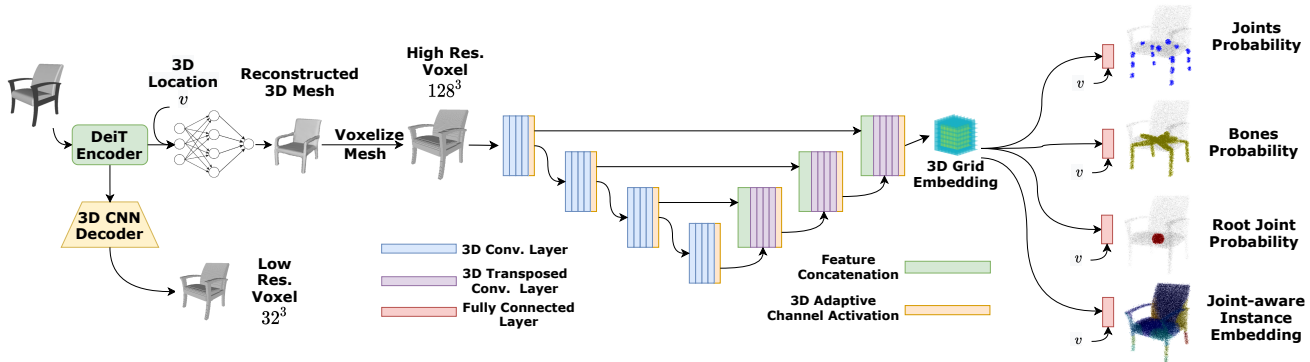


Figure 2. Our overall inference pipeline. It starts with the proposed Transformer-based model for 3D reconstruction. It consists of a DeiT image encoder, an auxiliary 3D CNN voxel prediction branch and the occupancy decoder. The SkelNet accepts the high resolution voxelized input from the reconstructed 3D mesh, and predict rigging required information with the multi-task architecture.

struction & animation to reconstruct & articulate generic lifeless objects from single images.

3. Our Approach

Given an input image, usually in the form of a segmented object, our approach consists of the following three steps. The 3D object shape is to be reconstructed; its skeletons are then extracted to form a rigged model; finally, various animations could be obtained by deforming the object with re-targeting source motions of humans or animals. Our emphasis in this paper is on the first two steps.

3.1. Step 1: Image-based 3D Shape Reconstruction

A Transformer-based occupancy prediction network is developed here, which performs particularly well on real images when compared with existing methods [16, 20, 40]. As illustrated in Fig. 2, it consists of a 2D transformer encoder, an auxiliary 3D CNN decoder, and an occupancy decoder. The DeiT-Tiny [33] is used as our transformer encoder network. Similar to the Vision Transformer [7], the encoder first encodes fixed-size patches splitted from the original image and processes extract localized information from each of the patches, then outputs a universal latent representation for the entire image by jointly learning the patch representation with multi-head attention. The auxiliary 3D CNN decoder is used for reconstructing a low-resolution voxel-based 3D model as well as helping to encode 3D information for the latent representation extracted from the Transformer encoder. The occupancy decoder then uses the latent representation as the conditional prior to predict the occupancy probability for each point by introducing fully connected residual blocks and conditional batch normalization [23, 26].

It is worth noting that although the voxel prediction branch is only used for auxiliary training, the highly unbalanced labels where most of the voxel occupancy are zeros will always make the training more difficult. To this end, while most of the methods for voxel-based 3D reconstruction

simply use the (binary) cross-entropy loss which is directly related to IoU metric [31], in this work, the Dice loss is extended to gauge on both the 3D voxel prediction and the point-based occupancy prediction,

$$\mathcal{L}_{dice} = 1 - \frac{\sum_{n=1}^{N^3} \hat{y}_n y_n}{\sum_{n=1}^{N^3} \hat{y}_n + y_n} - \frac{\sum_{n=1}^{N^3} (1 - \hat{y}_n)(1 - y_n)}{\sum_{n=1}^{N^3} 2 - \hat{y}_n - y_n}, \quad (1)$$

where y_n is the ground-truth occupancy score, \hat{y}_n is the predicted occupancy score of the n -th element.

3.2. Step 2: Skeleton Prediction

Our key insight here is instead of predicting the joints inside fixed voxel locations [43] or indirectly regressing the joints location by estimating the displacement from the mesh [42], we train a neural network utilizing the deep implicit function to assign every location with a probability score in $[0, 1]$, indicating the existence of a skeletal joint and bone. Taking the 3D model and any sampled 3D point location as input, the network produces the joint and bone existence probabilities. In addition, we incorporate joint-aware instance segmentation as an auxiliary task considering the regional features over neighboring points. In inference, the feature embedding output from the instance segmentation branch is further used in the subsequent step to infer joint locations from the incurred joints' probability maps.

As in Fig. 2, four output heads are utilized, which are for predicting the probability of skeletal joints, the root joint, the bones, and the joint-aware instance segmentation, respectively. The output from the instance segmentation is a feature embedding.

Feature Extraction. The predicted 3D shape, represented as an occupancy grid with the dimension of 128^3 is converted to a 3D feature embedding grid by a 3D UNet structure. Inspired by the design of Squeeze and Excitation (SE) block in 2D image classification, a 3D adaptive channel activation module is developed as a plug-in module, to be attached after each of the encoder and decoder block of the 3D UNet, as shown in Fig. 2. Empirical ablative study

demonstrated the usefulness of this 3D adaptive channel activation module.

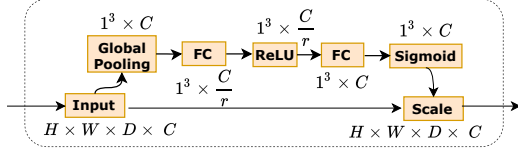


Figure 3. The 3D adaptive channel activation module.

Multi-head Implicit Functions. Given aggregated features from the feature extraction, we acquire the feature vector for any 3D point v via the trilinear interpolation from 3D feature embedding. For each of the output heads, a fully-connected network (empirically it is implemented as 5 fully-connected ResNet blocks and ReLU activation [23, 26]) is engaged to take as input the point v and its feature vector. The concurrent multi-head strategy eliminates the possible issue with error propagation of successive prediction [42].

Sampling. In general, the animation joints and bones should lie inside the convex hull of the object. Therefore, different from previous efforts that uniformly sample points in a 3D volume [20, 26], points in our 3D space are adaptively sampled. Specifically, for each sample in the training batch, we sampled K points with 10% of the points lying outside but near the surface, and the rest 90% points entirely inside the object.

Joints and Bones Loss. First, for every query point, its joint probability is computed under a 3D Gaussian distribution measured by its distance to nearest annotated joint locations. To generate the bone probability field, for every query point we compute a point-to-line distance to its nearest line segment of the bones, and the bone probability is computed under the Gaussian distribution of the measured distance. In training, with the query points $v \in \mathbb{R}^3$ acquired through sampling, the network predicts their probabilities of being a joint or lying on bones. Different from the occupancy prediction [20] task where the binary cross-entropy loss is used, we use the L1 loss to measure the difference of the predicted joint probability and their ground-truth values as we are dealing with the continuous probability prediction: for the i -th sample in training, the loss function is defined as,

$$\begin{aligned} \mathcal{L}_{joint}^i(\hat{P}_J, P_J) &= \sum_{v \in \mathcal{V}^i} |\hat{P}_J(v) - P_J(v)| \\ \mathcal{L}_{jointR}^i(\hat{P}_{JR}, P_{JR}) &= \sum_{v \in \mathcal{V}^i} |\hat{P}_{JR}(v) - P_{JR}(v)| \end{aligned} \quad (2)$$

where \hat{P}_J is the predicted joints probability field, and P_J is the ground-truth probability field. \hat{P}_{JR} and P_{JR} denote for the probability field of the root joint. \mathcal{V}^i denotes the sampled points for the i -th model.

Similarly, for the sampled points, L1 loss is also applied between predicted bones probability \hat{P}_B and the ground-truth P_B . The loss function of the bones is denoted as $\mathcal{L}_{bone}^i(\hat{P}_B, P_B)$.

Symmetry Loss. Since the objects of interest often possess symmetric 3D shapes, a symmetry loss is used here to regularize the solution space, as follows,

$$\begin{aligned} \mathcal{L}_{symJ}^i(\hat{P}_J) &= \mathbf{1}_{\Omega'}(i) \sum_{v \in \mathcal{V}^i} |\hat{P}_J(v) - \hat{P}_J(\phi(v))|, \\ \mathcal{L}_{symB}^i(\hat{P}_B) &= \mathbf{1}_{\Omega'}(i) \sum_{v \in \mathcal{V}^i} |\hat{P}_B(v) - \hat{P}_B(\phi(v))|, \end{aligned} \quad (3)$$

where $\phi(v)$ denotes the mapping from point v to its symmetric point. To detect the symmetry planes, as the input 3D mesh models are in the canonical coordinates, we flip the mesh model according to the xy -, xz - and yz -planes. The symmetry plane is set as the one with the smallest Chamfer distance computed between the flipped model and the original model. $\mathbf{1}_{\Omega'}$ is an indicator function where Ω' is the subset of training models with symmetry planes detected.

Joint-aware Instance Segmentation Loss. The joint-aware instance segmentation maps the sampled point from Euclidean space to a feature space, where 3D points of the same instance are closer to each other than those belonging to different instances. To maintain consistency between the clustered feature space and the joints probability maps, the part instance is segmented according to the annotated ground-truth joints. Basically, for each sampled point we assign an instance label as the label or index of its closest joint. Following the instance segmentation method of [38], our joint-aware instance segmentation loss is defined as a weighted sum of three terms: (1) \mathcal{L}_{var} is an intra-cluster variance term that pulls features belonging to the same instance towards the mean feature; (2) \mathcal{L}_{dist} is an inter-cluster distance term that pushes apart instances with different part labels; and (3) \mathcal{L}_{reg} is a regularization term that pulls all features towards the origin in order to bound the activation.

$$\begin{aligned} \mathcal{L}_{var}^i(\mu, x) &= \frac{1}{|J^i|} \sum_{c=1}^{|J^i|} \frac{1}{N_c} \sum_{j=1}^{N_c} [\|\mu_c^i - x_j^i\| - \delta_{var}]_+^2, \\ \mathcal{L}_{dist}^i(\mu) &= \frac{1}{|J^i|(|J^i| - 1)} \sum_{c_a=1}^{|J^i|} \sum_{\substack{c_b=1 \\ c_b \neq c_a}}^{|J^i|} [2\delta_{dist} - \|\mu_{c_a}^i - \mu_{c_b}^i\|]_+^2, \\ \mathcal{L}_{reg}^i(\mu) &= \frac{1}{|J^i|} \sum_{c=1}^{|J^i|} \|\mu_c^i\|. \end{aligned} \quad (4)$$

Here $|J^i|$ denotes the number of joints or clusters for the i -th sample model. N_c is the number of elements in cluster c . x_j^i is the output feature vector for the query point. $[x]_+$ is the hinge function. The parameter δ_{var} describes the maximum allowed distance between a feature vector and

the cluster center. Likewise, $2\delta_{dist}$ is the minimum distance between different cluster centers to avoid overlap.

Joints and Kinematic Tree Construction. In inference, the joints and bones are obtained from the corresponding probability maps by mean-shift clustering. Instead of clustering over the euclidean space as in classical mean-shift clustering, we implement the clustering on the feature space with the kernel defined over the feature embedding output from the joint-aware instance segmentation. In this way, the points belonging to the same joint-aware instance will all shift towards the corresponding joints. The kernel is also modulated by the predicted joint probability to better localize the joint location. Mathematically, at each mean-shift iteration, for any point v it is displaced according to the following vector:

$$m(v) = \frac{\sum_{u \in \mathcal{N}(v)} P_J(v) \kappa(\|x(u) - x(v)\|) u}{\sum_{u \in \mathcal{N}(v)} P_J(v) \kappa(\|x(u) - x(v)\|)} - v \quad (5)$$

where $\mathcal{N}(v)$ denotes the neighboring points of v , $x(v)$ is the feature embedding output from our joint-aware instance segmentation. Besides, $\kappa(\cdot)$ is a kernel function and in our case we choose to use the RBF kernel. Following [43], the object kinematic tree (or chains) are constructed using a minimum spanning tree by minimizing a cost function defined over the edges connecting the joints pair-wisely. It is realized as a graph structure, with the detected joints as the graph nodes, and the edges connecting the pairwise joints computed from the probability maps. Specifically, for every edge, its weight is set by the negative-log function of the integral of the bones probability for the sampled points over the edge. The MST problem is solved using Prim’s algorithm [6].

3.3. Step 3: Animation

For animation, the last issue is to compute the skinning weights that bind each vertex to the skeletal joints. To get meaningful animation, instead of computing the skinning weights according to the Euclidean distance [3], we choose to assign the skinning weights by utilizing the semantic part segmentation [38]. Specifically, for every segmented part, we assign its dominant control joint to the one closest to the center of the part, after which the skinning weights around the segmentation boundaries are smoothed out.

3.4. Our In-house Datasets

As there is no existing dataset of general 3D objects with ground-truth skeletons, we collect such a dataset (named SSkel for *ShapeNet skeleton*) by designing an annotation tool to place joints and build kinematic trees for the 3D shapes. To ensure consistency, a predefined protocol is used for all object categories. For example, for chairs, we follow the part segmentation in PartNet dataset [22] to segment a chair into the chair seat, back, and legs. The root

joint is annotated at the center of the chair seat, followed by child joints which are the intersection between chair seat and back, chair seat and legs. More details about the annotation tool and some sampled annotations are presented in the supplementary. Without loss of generality, we only consider four categories of objects from ShapeNet [4], namely *chair*, *table*, *lamp* and *airplane*. Our SSkel dataset contains a total of 2,150 rigged 3D shapes including 700 for chair, 700 for table, 400 for lamp and 350 for airplane.

Moreover, in improving the input image resolution and quality of the original ShapeNet, we use the UN-REAL 4 Engine to re-render photo-realistic images of the 3D ShapeNet models with diverse camera configuration, lighting conditions, object materials, and scenes, named ShapeRR dataset for *ShapeNet of realistic rendering*. More details are relegated to the supplementary file.

4. Experiments

Implementation Details. The object is first masked out with image segmentation and our reconstructed 3D model is further refined and deformed according to the object silhouettes. But for a fair comparison, the refinement is not applied for the reconstruction evaluation. To obtain the texture map of the reconstructed 3D model, we apply mirror texture for the invisible part.

Datasets. A number of datasets are considered in our paper. In terms of image-based reconstruction, it contains our ShapeRR dataset for synthetic images and the Pix3D dataset of real images. In terms of rigging performance, we use the RigNetv1 dataset for 3D shape based rigging, and our SSkel dataset for image-based rigging. The Pix3D dataset contains 3D object shapes aligned with their real-world 2D images. Similar to ShapeRR, we focus on a subset of 4 categories in the dataset, i.e. chair, sofa, desk, and table. The RigNetv1 dataset (i.e. ModelsResource-RigNetv1 [43]), on the other hand, contains 2,703 rigged 3D characters of humanoids, quadrupeds, birds, fish, robots, and other fictional characters.

4.1. Evaluation on Image-based Reconstruction

For evaluation metrics, we follow the previous works [20] and use volumetric IoU and Chamfer-L1 distance. We first compare with several state-of-the-art methods on single image object reconstruction where each of the methods is trained and tested on the ShapeNet dataset, namely OccNet [20], DVR [23] and D²IM-Net [16]. We follow the common test protocol on ShapeNet as it has been a standard benchmark in the literature. All methods are re-implemented (when the code is not available) and re-trained then evaluated directly on the test split. We can observe that our method performs reasonably well compared with other recent methods, and outperforms existing methods in 3 of the 4 categories. And we are able to achieve a significant

ShapeNet	Chamfer Distance (\downarrow)					Volumetric IoU (\uparrow)				
	Chair	Table	Lamp	Airplane	Avg.	Chair	Table	Lamp	Airplane	Avg.
OccNet [20]	1.9347	1.9903	4.5224	1.3922	2.3498	0.5067	0.4909	0.3261	0.5900	0.4918
DVR [23]	1.9188	2.0351	4.7426	1.3814	2.5312	0.4794	0.5439	0.3504	0.5741	0.5029
D ² IM-Net [16]	1.8847	1.9491	4.1492	1.4457	2.0346	0.5487	0.5332	0.3755	0.6123	0.5231
Ours	1.8904	1.7392	3.9712	1.2309	1.9301	0.5436	0.5541	0.3864	0.6320	0.5339
Pix3D	Table	Chair	Desk	Sofa	Avg.	Table	Chair	Desk	Sofa	Avg.
OccNet [20]	7.313	9.375	15.392	13.996	10.073	0.223	0.205	0.144	0.154	0.184
DVR [23]	8.394	6.283	12.344	11.345	9.702	0.193	0.243	0.169	0.189	0.182
D ² IM-Net [16]	7.943	7.386	10.956	8.977	8.472	0.201	0.250	0.182	0.209	0.215
Ours	6.227	4.833	7.398	6.983	6.998	0.247	0.291	0.223	0.245	0.247

Table 1. Image-based 3D mesh reconstruction on the ShapeRR (i.e. re-rendered ShapeNet dataset) and Pix3D dataset. Metrics are Chamfer Distance ($\times 0.001$, the smaller the better) and Volumetric IoU (the larger the better). Best results are in **bold face**.

ResNet	DeiT	Vox.	Dice	CD (\downarrow)	Vol. IoU (\uparrow)
\checkmark				2.1504	0.5014
	\checkmark			1.9801	0.5217
	\checkmark	\checkmark		1.9723	0.5268
	\checkmark	\checkmark	\checkmark	1.9301	0.5339

Table 2. Ablation study on the ShapeRR dataset to validate the effectiveness of each component in our image-based reconstruction step. Chamfer Distance (CD) and Volumetric IoU (Vol. IoU) are used as metrics.

advantage over other methods in terms of the average performance across all 4 categories of our interests.

Considering that our 3D reconstruction is primarily for supporting rigging and animation purposes on real images, to better compare the generalization ability with such a situation, we use the complete Pix3D dataset as the test set. Each of the objects in Pix3D comes with a group of photography, therefore for each object, we use all the related images and predict a 3D mesh for each of the input images. The final quantitative results for each category are calculated by the average of the best 3 reconstructed models with the smallest Chamfer Distance to the ground-truth. We report both quantitative and visual comparison on Pix3D in Table 1 and in Fig. 4 respectively. As shown in Table 1, our proposed method has outperformed all previous approaches on Pix3D with a large margin in terms of the two metrics.

Ablation study. For the sake of completeness, we also conduct a group of ablative studies on the components we have in the reconstruction model. First, we test different backbone architectures (i.e., ResNet and DeiT-Tiny) used in our method. We then perform a warm-up training by including the voxel prediction branch, after the warm-up training, the voxel branch is discarded. Lastly, we compare training with Dice loss and the ordinary binary cross-entropy loss. Brief quantitative results are demonstrated in Table 2.

	CD-J2J (\downarrow)	CD-B2B (\downarrow)
Pinocchio [3]	0.072	0.047
Volumetric [43]	0.045	0.026
RigNet [42]	0.039	0.022
Ours	0.029	0.017

Table 3. Rigging performance comparison on the RigNetv1 dataset.

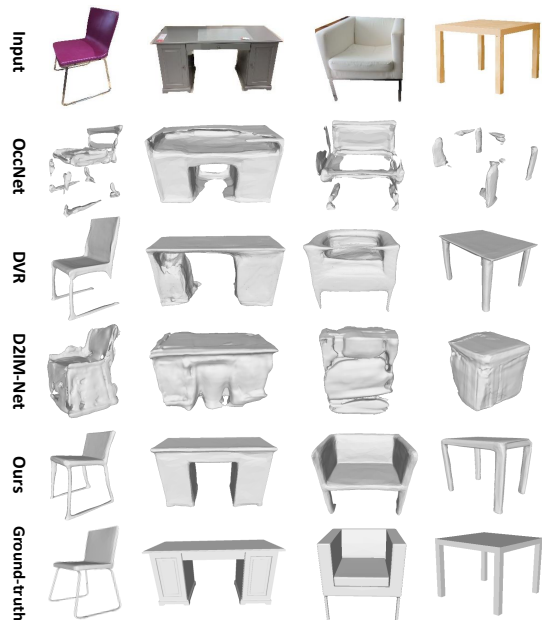


Figure 4. Visualizations of image-based 3D reconstruction on the Pix3D dataset. Our method shows excellent generalization performance on the real image input.

4.2. Evaluation on Rigging

The evaluation is conducted on both the RigNetv1 dataset and our SSkel dataset, where our approach is compared with two state-of-the-art methods, RigNet [42] and

metrics	Chair		Table		Lamp		Airplane		All	
	CD-J2J	CD-B2B								
RigNet [42]	0.052	0.035	0.061	0.040	0.132	0.098	0.096	0.073	0.061	0.041
Ours	0.030	0.021	0.044	0.028	0.097	0.063	0.075	0.056	0.047	0.033

Table 4. Quantitative comparison of skeletal joint prediction on our SSkel dataset. The CD-J2J & CD-B2B values are the smaller the better. Best results are in **bold face**.

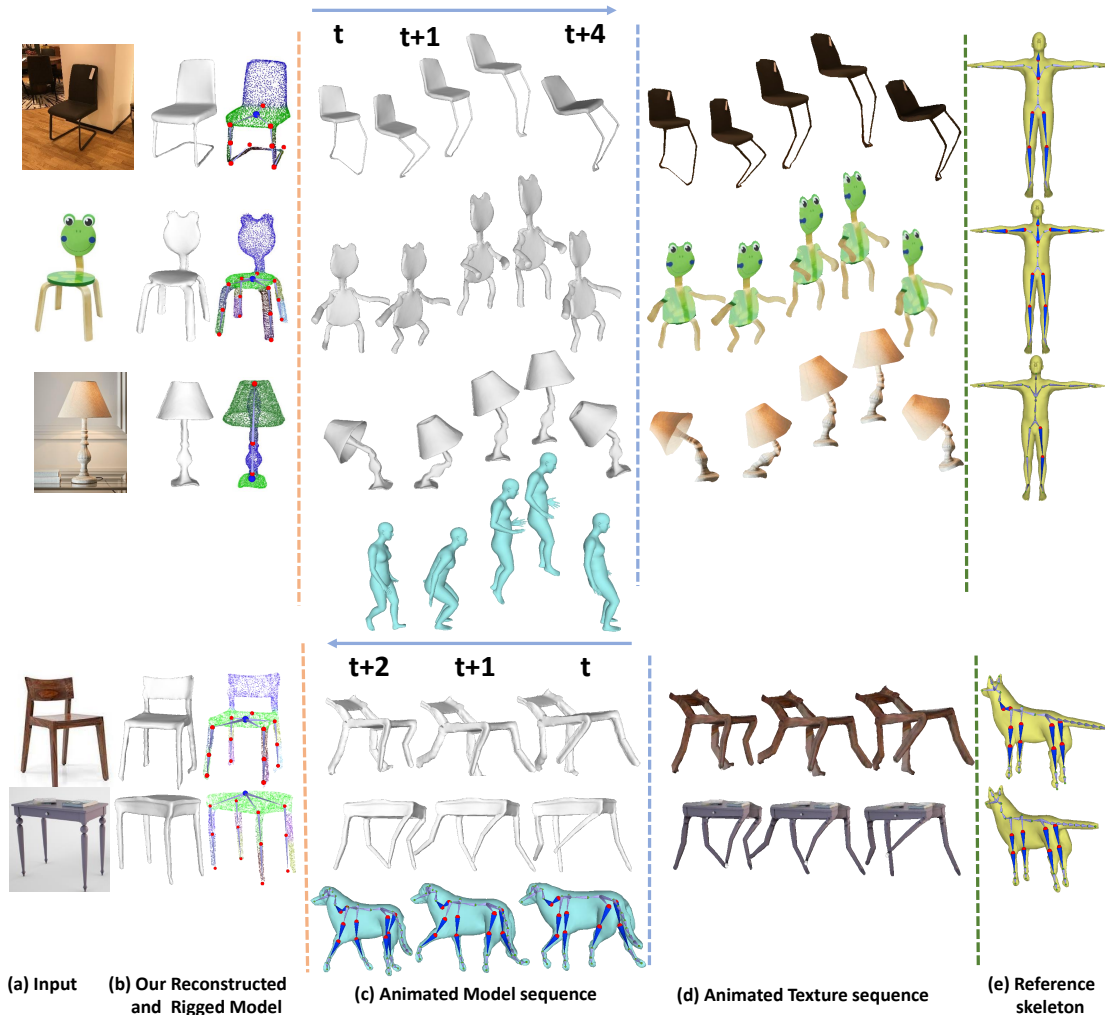


Figure 5. Animation results of our entire pipeline. Given an input image (i.e. the object segment), its 3D shape is reconstructed and rigged, followed by the animated sequence (re-targeted from human or quadruped motions, which is not the main focus of this work). We map the joints from the human or quadruped template skeleton to the objects with the mapped joints marked in red (c). The source human/dog motion is shown in the bottom row.

VolumetricNets [43].

Metrics. First, we measure the accuracy of the predicted joints by computing the Chamfer distance between the predicted joints and the ground-truth which is denoted as CD-J2J. Similarly, the predicted bones are evaluated by computing the Chamfer distance between the densely sampled points over the estimated bones and the ground-truth, which is denoted as CD-B2B. For both metrics CD-J2J and CD-

B2B, the lower the better.

Quantitative evaluation. In Table 3 and Table 4, we show the comparison results of the predicted skeleton on the RigNetv1 dataset [43] and our SSkel dataset respectively. For the RigNetv1 dataset, we follow the same train and test split as previous works [42,43]. We have re-trained the RigNet [42], which is the most current work on auto-rigging, on our SSkel dataset. We report the skeleton er-

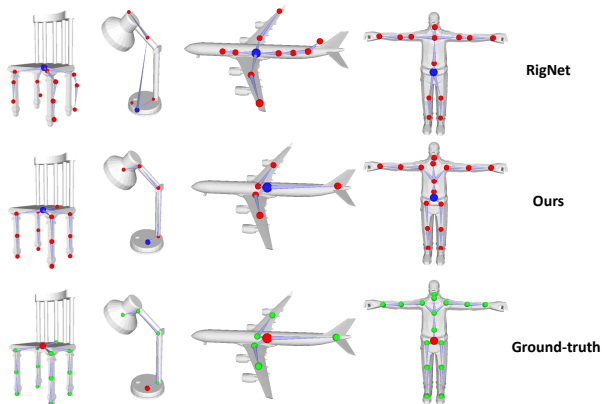


Figure 6. Visual comparison on skeleton prediction. The left three models are from SSKel dataset and the rightmost comes from the RigNetv1 dataset.

ror when trained separately on each category as well as trained on all categories together. As shown in the tables, our proposed skeleton prediction method has outperformed the current state-of-the-art approaches on both the RigNetv1 dataset and our SSKel dataset.

Visual results on skeleton prediction. In Fig. 6 we demonstrate the qualitative comparison of the predicted skeleton with the RigNet method [42]. As shown in the figure, compared with the most current work, our proposed approach can produce more reasonable results that correctly predicted the joints’ location and constructed the kinematic chains. On the other hand, the RigNet method fails to localize the joints. The reason is that their mesh-based approach requires the vertices to be evenly distributed over the mesh and they rely on the mesh curvature to pre-train an attention model. But for the models from the SSKel dataset, there is no close connection between the mesh curvature and the joint locations. More visual results can be found in the supplementary.

Ablation study. To validate the effectiveness of several key components of the proposed method, we conduct several ablation studies with the quantitative evaluation results shown in Table 5. We denote our method without the 3D channel adaptive activation, symmetry loss, and joint-aware instance segmentation as the Baseline method.

	RigNetv1	SSkel
Baseline	0.037	0.065
Baseline + joint-aware seg	0.033	0.055
Baseline + symmetry loss	0.034	0.058
Baseline + 3D adaptive activation	0.033	0.056
Ours	0.029	0.047

Table 5. Ablation study on joints prediction. CD-J2J metric is used.

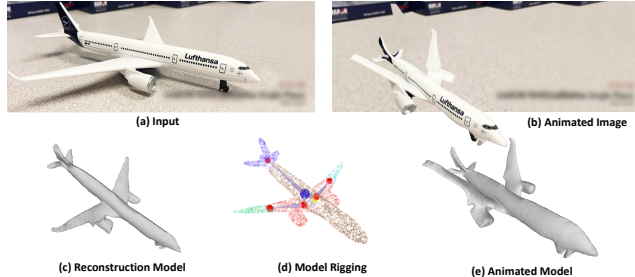


Figure 7. An visual airplane running example of executing our entire pipeline: (a) input image; (c) our reconstructed 3D mesh; (d) semantic segmentation, and the predicted skeletal joints; (e) our 3D animated mesh; and finally, (b) our rendered image in the original image space.

4.3. Animation Results of our Pipeline

In this section, we conduct the animation for various objects from input images. In Fig. 5, we demonstrate the animation of objects as driven by the source motion of reference articulated models. Specifically, in the upper rows of Fig. 5 we map the motion of a Jumping human to two Chairs as well as a Lamp. The details of the skeleton mapping from the human template to the animated objects are shown in each corresponding row of Fig. 5(d). Likewise, in the lower part of Fig. 5, we demonstrate the manipulation of one Chair and Table driven by a quadruped. It is conducted by mapping the joints of four legs on the Dog skeleton to the legs of the chair and table. In addition, the joint of the neck is mapped to the joint on the chair back. The motion sequence of the dog is from the RGBD-Dog dataset [13].

Furthermore, in Fig. 7, we demonstrate the manipulation of an airplane. By adjusting the angle of the two wings as well as the global transformation, we achieve the final animation effect with the airplane flying over the floor as shown in Fig. 7(b).

5. Conclusion and Limitations

We consider an interesting task of waking up a 3D object from a single input image. An automated pipeline is proposed to reconstruct the 3D object, predict the animation skeleton for the 3D model and finally animate the object with plausible articulations. Quantitative and qualitative experiments demonstrate the applicability of our work when unseen real-world images are presented at test time.

Limitations. Although we have achieved the best reconstruction performance on real images, the domain gap between synthetic to real images still exists. Moreover, the collected SSKel dataset is limited in the number of objects and the range of object categories. For future work, we plan to explore its applicability in working with a much broad range of object categories and a larger number of annotated objects.

References

- [1] Nina Amenta and Marshall Bern. Surface reconstruction by voronoi filtering. *Discrete & Computational Geometry*, 22(4):481–504, 1999. [2](#)
- [2] Dominique Attali and Annick Montanvert. Computing and simplifying 2D and 3D continuous skeletons. *Computer Vision and Image Understanding*, 67(3):261–273, 1997. [2](#)
- [3] Ilya Baran and Jovan Popović. Automatic rigging and animation of 3d characters. *ACM Transactions on graphics(TOG)*, 26(3):72, 2007. [2](#), [5](#), [6](#)
- [4] Angel X Chang, Thomas Funkhouser, Leonidas Guibas, Pat Hanrahan, Qixing Huang, Zimo Li, Silvio Savarese, Manolis Savva, Shuran Song, Hao Su, et al. Shapenet: An information-rich 3D model repository. *arXiv preprint arXiv:1512.03012*, 2015. [5](#)
- [5] Zhiqin Chen and Hao Zhang. Learning implicit fields for generative shape modeling. In *IEEE/CVF Conference on Computer Vision and Pattern Recognition*, 2019. [2](#)
- [6] David Cheriton and Robert Endre Tarjan. Finding minimum spanning trees. *SIAM Journal on Computing*, 5(4):724–742, 1976. [5](#)
- [7] Alexey Dosovitskiy, Lucas Beyer, Alexander Kolesnikov, Dirk Weissenborn, Xiaohua Zhai, Thomas Unterthiner, Mostafa Dehghani, Matthias Minderer, Georg Heigold, Sylvain Gelly, et al. An image is worth 16x16 words: Transformers for image recognition at scale. In *International Conference on Learning Representations (ICLR)*, 2021. [3](#)
- [8] Haoqiang Fan, Hao Su, and Leonidas J Guibas. A point set generation network for 3d object reconstruction from a single image. In *IEEE Conference on Computer Vision and Pattern Recognition*, 2017. [2](#)
- [9] Georgia Gkioxari, Jitendra Malik, and Justin Johnson. Mesh R-CNN. In *IEEE/CVF International Conference on Computer Vision*, 2019. [2](#)
- [10] Alexander Hornung, Ellen Dekkers, and Leif Kobbelt. Character animation from 2d pictures and 3d motion data. *ACM Transactions on Graphics(TOG)*, 26(1):1, 2007. [2](#)
- [11] Hui Huang, Shihao Wu, Daniel Cohen-Or, Minglun Gong, Hao Zhang, Guiqing Li, and Baoquan Chen. L1-medial skeleton of point cloud. *ACM Transactions on Graphics (TOG)*, 32(4):65–1, 2013. [2](#)
- [12] Hiroharu Kato, Yoshitaka Ushiku, and Tatsuya Harada. Neural 3d mesh renderer. In *IEEE Conference on Computer Vision and Pattern Recognition*, 2018. [2](#)
- [13] Sinead Kearney, Wenbin Li, Martin Parsons, Kwang In Kim, and Darren Cosker. Rgb-dog: Predicting canine pose from rgb-d sensors. In *IEEE/CVF Conference on Computer Vision and Pattern Recognition*, pages 8336–8345, 2020. [8](#)
- [14] Natasha Kholgade, Tomas Simon, Alexei Efros, and Yaser Sheikh. 3d object manipulation in a single photograph using stock 3D models. *ACM Transactions on Graphics (TOG)*, 33(4):1–12, 2014. [1](#), [2](#)
- [15] Dominik Kulon, Riza Alp Guler, Iasonas Kokkinos, Michael M Bronstein, and Stefanos Zafeiriou. Weakly-supervised mesh-convolutional hand reconstruction in the wild. In *IEEE/CVF Conference on Computer Vision and Pattern Recognition*, 2020. [2](#)
- [16] Manyi Li and Hao Zhang. D2im-net: Learning detail disentangled implicit fields from single images. In *IEEE/CVF Conference on Computer Vision and Pattern Recognition*, pages 10246–10255, 2021. [3](#), [5](#), [6](#)
- [17] Chen-Hsuan Lin, Chen Kong, and Simon Lucey. Learning efficient point cloud generation for dense 3D object reconstruction. In *AAAI Conference on Artificial Intelligence*, 2018. [2](#)
- [18] Chen-Hsuan Lin, Chaoyang Wang, and Simon Lucey. Sdf-srn: Learning signed distance 3D object reconstruction from static images. In *Advances in Neural Information Processing Systems*, 2020. [2](#)
- [19] Shichen Liu, Tianye Li, Weikai Chen, and Hao Li. Soft rasterizer: A differentiable renderer for image-based 3d reasoning. In *IEEE/CVF International Conference on Computer Vision*, 2019. [2](#)
- [20] Lars Mescheder, Michael Oechsle, Michael Niemeyer, Sebastian Nowozin, and Andreas Geiger. Occupancy networks: Learning 3d reconstruction in function space. In *IEEE/CVF Conference on Computer Vision and Pattern Recognition*, 2019. [1](#), [2](#), [3](#), [4](#), [5](#), [6](#)
- [21] Zhenxing Mi, Yiming Luo, and Wenbing Tao. Ssrnet: scalable 3D surface reconstruction network. In *IEEE/CVF Conference on Computer Vision and Pattern Recognition*, 2020. [2](#)
- [22] Kaichun Mo, Shilin Zhu, Angel X Chang, Li Yi, Subarna Tripathi, Leonidas J Guibas, and Hao Su. Partnet: A large-scale benchmark for fine-grained and hierarchical part-level 3d object understanding. In *IEEE/CVF Conference on Computer Vision and Pattern Recognition*, 2019. [5](#)
- [23] Michael Niemeyer, Lars Mescheder, Michael Oechsle, and Andreas Geiger. Differentiable volumetric rendering: Learning implicit 3D representations without 3D supervision. In *IEEE/CVF Conference on Computer Vision and Pattern Recognition*, 2020. [3](#), [4](#), [5](#), [6](#)
- [24] Junyi Pan, Xiaoguang Han, Weikai Chen, Jiapeng Tang, and Kui Jia. Deep mesh reconstruction from single rgb images via topology modification networks. In *IEEE International Conference on Computer Vision*, 2019. [2](#)
- [25] Jeong Joon Park, Peter Florence, Julian Straub, Richard Newcombe, and Steven Lovegrove. Deepsdf: Learning continuous signed distance functions for shape representation. In *IEEE/CVF Conference on Computer Vision and Pattern Recognition*, 2019. [2](#)
- [26] Songyou Peng, Michael Niemeyer, Lars Mescheder, Marc Pollefeys, and Andreas Geiger. Convolutional occupancy networks. In *European Conference on Computer Vision (ECCV)*, pages 523–540, 2020. [3](#), [4](#)
- [27] Charles R Qi, Li Yi, Hao Su, and Leonidas J Guibas. Pointnet++: Deep hierarchical feature learning on point sets in a metric space. In *Advances in Neural Information Processing Systems*, 2017. [2](#)
- [28] Gernot Riegler, Ali Osman Ulusoy, and Andreas Geiger. Octnet: Learning deep 3D representations at high resolutions. In *IEEE Conference on Computer Vision and Pattern Recognition*, 2017. [2](#)

- [29] Scott Schaefer, Travis McPhail, and Joe Warren. Image deformation using moving least squares. *ACM Transactions on Graphics(TOG)*, 25(3):533–540, 2006. 2
- [30] Ruoxi Shi, Zhengrong Xue, Yang You, and Cewu Lu. Skeleton merger: an unsupervised aligned keypoint detector. In *IEEE conference on computer vision and pattern recognition*, 2021. 2
- [31] Zai Shi, Zhao Meng, Yiran Xing, Yunpu Ma, and Roger Wattenhofer. 3d-retr: End-to-end single and multi-view 3D reconstruction with transformers. In *The British Machine Vision Conference*, 2021. 3
- [32] Maxim Tatarchenko, Alexey Dosovitskiy, and Thomas Brox. Octree generating networks: Efficient convolutional architectures for high-resolution 3d outputs. In *IEEE International Conference on Computer Vision*, 2017. 2
- [33] Hugo Touvron, Matthieu Cord, Matthijs Douze, Francisco Massa, Alexandre Sablayrolles, and Herve Jegou. Training data-efficient image transformers and distillation through attention. In *International Conference on Machine Learning*, volume 139, pages 10347–10357, 2021. 1, 3
- [34] Edgar Tretschk, Ayush Tewari, Vladislav Golyanik, Michael Zollhöfer, Carsten Stoll, and Christian Theobalt. Patchnets: Patch-based generalizable deep implicit 3d shape representations. In *European Conference on Computer Vision*, 2020. 2
- [35] Shubham Tulsiani, Alexei A Efros, and Jitendra Malik. Multi-view consistency as supervisory signal for learning shape and pose prediction. In *IEEE Conference on Computer Vision and Pattern Recognition*, 2018. 2
- [36] Nanyang Wang, Yinda Zhang, Zhuwen Li, Yanwei Fu, Wei Liu, and Yu-Gang Jiang. Pixel2mesh: Generating 3d mesh models from single rgb images. In *European Conference on Computer Vision*, 2018. 2
- [37] Peng-Shuai Wang, Yang Liu, and Xin Tong. Deep octree-based cnns with output-guided skip connections for 3D shape and scene completion. In *IEEE/CVF Conference on Computer Vision and Pattern Recognition Workshops*, 2020. 2
- [38] Weiyue Wang, Ronald Yu, Qiangui Huang, and Ulrich Neumann. Sgpn: Similarity group proposal network for 3d point cloud instance segmentation. In *Proceedings of the IEEE conference on computer vision and pattern recognition*, pages 2569–2578, 2018. 4, 5
- [39] Chung-Yi Weng, Brian Curless, and Ira Kemelmacher-Shlizerman. Photo wake-up: 3d character animation from a single photo. In *IEEE/CVF Conference on Computer Vision and Pattern Recognition*, pages 5908–5917, 2019. 1, 2
- [40] Qiangeng Xu, Weiyue Wang, Duygu Ceylan, Radomir Mech, and Ulrich Neumann. Disn: Deep implicit surface network for high-quality single-view 3d reconstruction. In *Advances in Neural Information Processing Systems*, 2019. 3
- [41] Xuemiao Xu, Liang Wan, Xiaopei Liu, Tien-Tsin Wong, Liansheng Wang, and Chi-Sing Leung. Animating animal motion from still. 27(5):1–8, 2008. 2
- [42] Zhan Xu, Yang Zhou, Evangelos Kalogerakis, Chris Landreth, and Karan Singh. Rignet: Neural rigging for articulated characters. *ACM Transactions on Graphics(TOG)*, 39(58), 2020. 2, 3, 4, 6, 7, 8
- [43] Zhan Xu, Yang Zhou, Evangelos Kalogerakis, and Karan Singh. Predicting animation skeletons for 3d articulated models via volumetric nets. In *International Conference on 3D Vision*, pages 298–307, 2019. 2, 3, 5, 6, 7
- [44] Kangxue Yin, Hui Huang, Daniel Cohen-Or, and Hao Zhang. P2p-net: Bidirectional point displacement net for shape transform. *ACM Transactions on Graphics (TOG)*, 37(4):1–13, 2018. 2